THE JOURNAL OF PHYSICAL CHEMISTRY C
A JOURNAL OF THE AMERICAN CHEMICAL SOCIETY

pubs.acs.org/JPCC

Article

Tuning the Polarity of Dinitrile-Based Electrolyte Solutions for CO_2 Electroreduction on Copper Catalysts

Tatiana Morin Caamano, Mohamed S. E. Houache, Mario G. Sandoval, Martin Couillard, Arnaud Weck, Elena. A. Baranova, and Yaser Abu-Lebdeh*

Cite This: *J. Phys. Chem. C* 2023, 127, 7230–7238

Read Online

ACCESS | Metrics & More | Article Recommendations | Supporting Information

ABSTRACT: The development of carbon dioxide electrochemical reduction (CO_2ER) has mainly focused on aqueous electrolytes. However, the low solubility of apolar CO_2 in polar water negatively impacts the electrochemical process, especially mass transport. Organic-based electrolytes, such as methanol, acetonitrile, and dimethylformamide, have been explored as an alternative due to increased CO_2 solubility. Yet, insights into other organic electrolytes are scarce. Dinitrile solvents have decreased polarity in comparison to the mononitrile solvent acetonitrile and thus can potentially further increase CO_2 solubility and advance the reaction's performance. Herein, the novelty of dinitrile-based electrolytes for the application of CO_2ER is explored. Acetonitrile, adiponitrile, and sebaconitrile were used to study the effects of a secondary nitrile group addition and the length of the aliphatic, nonpolar chain on salt solubility, electrolyte conductivity, and CO_2 solubility. Electrochemical effects were evaluated through cyclic voltammetry (CV) and chronoamperometry (CA) measurements with copper (Cu) and copper oxide (CuO) commercial nanoparticle catalysts. DFT calculations were employed to further explore the CO_2 interactions with the selected solvents. Finally, it was found that tuning the polarity of the nitrile solvent results in a profound effect on the physiochemical properties of the electrolyte solutions, markedly CO_2 solubility and the CO_2ER.

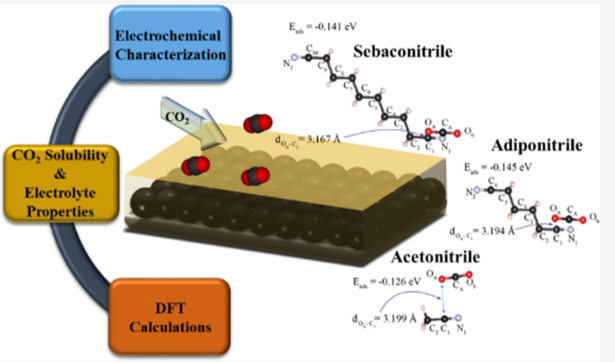

1. INTRODUCTION

The continual accumulation of carbon dioxide (CO_2) in the atmosphere due to anthropogenic sources has led to record levels of atmospheric global CO_2 average.[1,2] Due to the link of rising global temperatures to the increase of CO_2 accumulation since the beginning of the industrial age, this has led to the current climate crisis. The 2022 IPCC report has outlined that the world is on the path to reach a 1.5 °C increase in temperature in the next 20 years.[3] In order to avoid climate disasters associated with surpassing of this threshold, the development and implementation of sustainable alternative sources for fossil-derived fuels and feedstock chemicals has become crucial.[1]

Posing promising potential, is the CO_2 electrochemical reduction (CO_2ER) reaction by its ability to convert CO_2 to added value chemicals, such as energy-dense hydrocarbons like ethylene.[1,2] In combination with carbon capture and renewable energy sources, the reaction can become a net carbon zero process. Copper (Cu) has particularly been identified as a catalyst of importance for the reaction due to its unique ability to generate hydrocarbons.[1,2,4] Still, the technology continues to achieve commercial viability, as not only does Cu exhibit low selectivity but also does not possess sufficiently high activity and stability for efficient catalytic performance.[1,2,4]

Aqueous-based electrolytes, such as bicarbonate or phosphate-buffered solutions, are commonly used for the reaction.[5] They possess advantages such as low cost, wide availability, and low toxicity.[5,6] However, they exhibit low CO_2 solubilities, thus resulting in performance drawbacks due to mass-transfer limitations.[5,6] Organic solvent electrolytes have the advantage of possessing comparably higher CO_2 solubilities. In addition, due to the limitation of available protons in aprotic organic solvents, these also suppress the competing hydrogen evolution reaction (HER).[5,6] In aprotic electrolytes, the CO_2ER is also affected as it follows a different reaction pathway in aqueous solvents, that of the generation of the $CO_2^{-\bullet}$ anion radical, shown in eq 1.[5,6] From the anion radical, products such as CO, CO_3^{2-}, formate, and oxalate can then be formed.[5,6] Notably, the reaction occurs at more negative potentials compared to aqueous electrolytes, as it requires a standard potential of −1.85 V vs NHE.

Received: February 6, 2023
Revised: February 22, 2023
Published: April 5, 2023

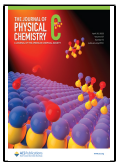

$$CO_2 + e^- \rightarrow CO_2^{-\bullet} \qquad E^0 = -1.85 \text{ V vs NHE} \qquad (1)$$

As a result, the Cu-catalyzed CO_2ER in organic electrolytes does not possess an extensive variety of reaction pathways as in the case of aqueous electrolytes and thus has better viability to achieve improved product selectivity. However, a trade-off that is to be considered is the requirement of more negative potentials to achieve the CO_2ER anion radical pathway.

Nitrile-based organic electrolytes, such as acetonitrile (ACN), are known to possess high thermal and electrochemical stability. Additionally, ACN displays a CO_2 solubility of 270 mM compared to that of 40 mM in water.[5] Notably, the solubility of apolar CO_2 has the potential to be further improved in nitrile-based solvents by tuning the polarity of aliphatic dinitrile solvents with the chemical formula N≡C−$(CH_2)_n$−C≡N, where (n) indicates the number of methylene groups in the chain. Therefore, the dinitrile polarity can be reduced through increasing the nonpolar component of the molecules by increasing n. An additional advantage of dinitrile solvents over mononitriles that are volatile in nature, such as ACN, is that the addition of another carbon−nitrogen bond (nitrile group) increases the cohesive energy of the molecules and hence reduces their volatility.

As such, this work demonstrates for the first time the effect of the use of organic dinitrile solvents with evaluation of the variation in the chain length of dinitrile compounds on CO_2 solubility for the application of CO_2ER. The selected solvents under study were acetonitrile, a studied mononitrile for comparison purposes, as well as two dinitriles, adiponitrile (n = 4), ADN, and sebaconitrile (n = 8), SEN. A supporting electrolyte, tetrabutylammonium hexafluorophosphate ($TBAPF_6$), was used due to its wide electrochemical potential window. Solubility limits of $TBAPF_6$ in the selected nitrile-based solvents were tested. Conductivity against concentration and temperature was also explored. Then, CO_2 solubility in the organic solvents was measured. Performance on CO_2ER was studied with the use of commercial copper-based catalysts through cyclic voltammetry (CV) and chronoamperometry (CA) measurements. Finally, a DFT analysis of the interactions between CO_2 and the nitrile solvents was carried out to understand the CO_2 solubility effects.

2. EXPERIMENTAL SECTION

2.1. Chemicals. Copper nano-powder (Cu NPs, 25 nm particle size, TEM) was purchased from Sigma-Aldrich. CuO nano-powder (CuO NPs, 40 nm, TEM) was purchased from US Research Nanomaterials Inc. The organic solvents consisted of acetonitrile (ACN, >99.9%, Sigma-Aldrich, USA), adiponitrile (ADN, 99%, Sigma-Aldrich, USA), and sebaconitrile (SEN 95%, Alfa Aesar, USA). The solvents were dried for 7 days using 3A, 3.2 mm pellet molecular sieves (Sigma-Aldrich, USA). Tetrabutylammonium hexafluorophosphate ($TBAPF_6$, >99%, Sigma-Aldrich, USA) salts were dried in a vacuum oven at a temperature of 90 °C overnight. After drying, the organic electrolytes were prepared with 0.1 M $TBAPF_6$ and 5 mM ferrocene (98%, Sigma, USA) in ACN and/or SEN. The aqueous electrolyte was a solution of aqueous 0.1 M potassium bicarbonate ($KHCO_3$, 99%, Alfa Aesar, USA) in deionized water (Milli-Q Millipore, 18.2 MΩ cm at 293 K).

2.2. Physiochemical Characterization. CO_2 solubility was quantitatively compared between the organic solvents using collected Fourier-transform infrared (FTIR) spectroscopy.[7] A Nicolet 6700 FTIR spectrometer from Thermo Scientific equipped with a zinc selenide sample holder was used for ATR FTIR collection. The scanning range of the spectrum was 4000−650 cm^{-1}. The spectra were analyzed using the Omnic software. From the resulting peak characteristic of CO_2, the areas were integrated using OriginPro between the spectrum of 2200−2400 cm^{-1}. The resulting areas were normalized over the integrated peak of anhydrous ethanol reference between the bounds of 2200−4000 cm^{-1}. Then, the Beer−Lambert formula, shown by eq 2, was utilized to estimate the CO_2 concentration with the use of the absorbance normalized area

$$A = \varepsilon b C \qquad (2)$$

where A is the absorbance, ε is the molar absorptivity coefficient, b the length of light path, and C is the concentration. X-ray powder diffraction (XRD) was used to analyze the composition and crystalline structure of the nanoparticles. XRD studies were conducted with a Rigaku Ultima IV PXRD system under copper K radiation (λ = 1.5418 Å) set to 40 kV/44 mA. The scanning 2θ range was 20−80° with a step of 0.1°. Transmission electron microscopy (TEM) was conducted using JEM-2100F or FEI Titan-3 80−300 microscope. Conductivity was measured using a Russel RL060C Portable Conductivity Meter (Thermo Scientific, USA). Solubility was determined by adding small amounts of $TBAPF_6$ to a known volume of each solvent and manually mixing until failure to dissolve.

2.3. Electrochemical Characterization. A three-electrode cell setup with ∼60 mL of electrolyte was utilized. The electrochemical cell body consisted of a small-volume quartz glass cell (Pine Research, USA). The reference electrode consisted of a Ag/Ag^+ nonaqueous pseudo-reference electrode (ALS Co., Japan) filled with 0.1 M $TBAPF_6$ and 10 mM $AgNO_3$ in acetonitrile. For the counter electrode, a Pt mesh was used (ALS Co., Japan). The working electrode consisted of 2 μL of particle catalyst ink deposited on an L-shaped glassy carbon electrode (3 mm diameter, DEK Research). An image of the assembled electrochemical cell is presented in the Supporting Information, Figure S1. The catalyst ink was prepared with 6 mg of particle powder, 1 mL of deionized water (18 MΩ), 200 μL of isopropanol, and 100 μL of Nafion (∼5%, Sigma Aldrich, USA) mixed by sonication for approximately 5 min. Prior to deposition, the working electrode surface was polished with 30 and 5 μm alumina, rinsed with ethanol and then deionized water. For the reference electrode calibration, the Ag/Ag^+ nonaqueous reference electrode was calibrated against the redox half potential of ferrocene. 5 mM ferrocene was included in the electrolyte solution as internal reference and was calibrated before every new catalyst deposition run. Details pertaining to the calibration procedure are depicted in the Supporting Information, Figure S2. Cyclic voltammetry (CV) experiments were conducted from a range between −0.8 and −1.82 V vs NHE with a step size of 50 mV/s. The cycles were repeated 5 times, and the last cycle was evaluated. The tests were conducted first after 20 min of N_2 purge and again after 15 min of CO_2 purge. The chronoamperometry (CA) tests were conducted with a held potential of −1.7 V vs NHE for 3 h while maintaining CO_2 purging. After the CA tests, another CV trial was conducted at the mentioned conditions under CO_2 purge.

https://doi.org/10.1021/acs.jpcc.3c00819
J. Phys. Chem. C 2023, 127, 7230−7238

Table 1. Electrolyte Properties of Water and Evaluated Nitrile Solvents[8a]

Electrolyte	Structure	ε	η (cP)	T_m (°C)	T_b (°C)	T_f (°C)	T_{auto} (°C)
Water		80[9]	1	0	100	-	-
Acetonitrile		37	0.3	-48	81	2	523
Adiponitrile	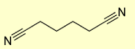	30	6.1	1	295	163	550
Sebaconitrile	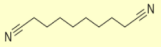	22	10.7	8	200	>113	-

[a] ε = dielectric constant, η = dynamic viscosity, T_m = melting-point temperature, T_b = boiling-point temperature, T_f = flash-point temperature, and T_{auto} = autoignition temperature.

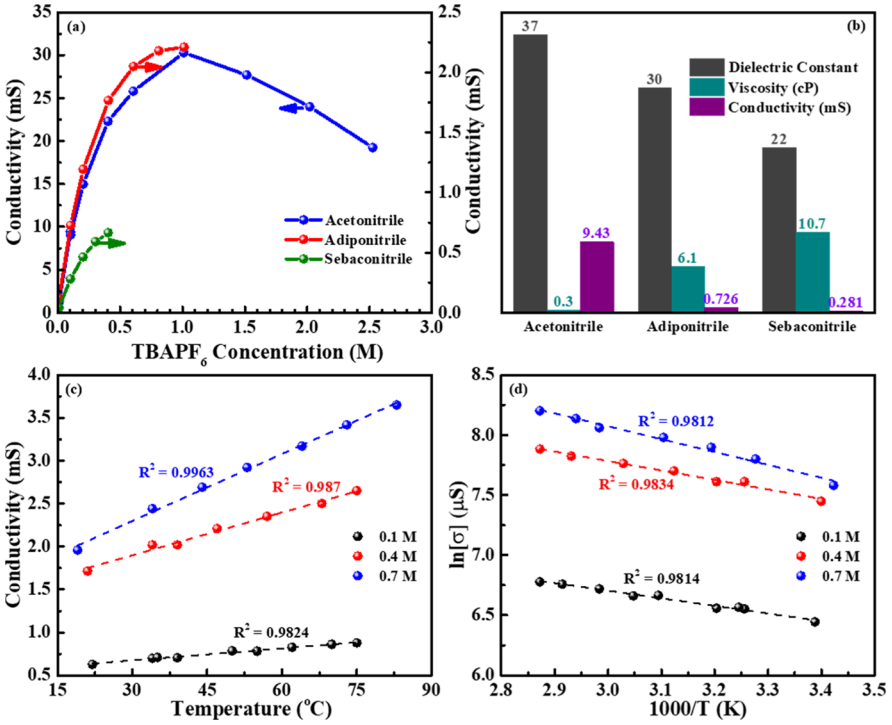

Figure 1. Behavior of (a) electrolyte conductivity versus $TBAPF_6$ concentration, (b) dielectric constant and viscosity relationship with 0.1 M electrolyte solution conductivity for ACN, ADN, and SEN solvents. Behavior of (c) conductivity versus temperature and (d) linearized Arrhenius plot derived from the conductivity versus temperature data for ADN solutions at different $TBAPF_6$ concentrations.

2.4. Computational Methods. All detailed procedures of the density functional theory (DFT) calculations are reported in the Supporting Information.

3. RESULTS AND DISCUSSION

3.1. Electrolyte Properties, Conductivity, and Solubility. Select properties for all evaluated solvents are shown in Table 1. It can be observed that the dinitrile solvents possess higher boiling points to water and ACN. Additionally, the dinitriles demonstrate lower flammability and higher flash points compared to ACN. A decreasing dielectric constant trend can also be observed following the order of water > ACN > ADN > SEN. As the dielectric constant is a measure of the polarity of a molecule, the observed trend exhibited by the organic solvents shows evidence that the polarity of the solvents is reduced with the addition of a second nitrile (−CN) group, as well as with added methylene ($-CH_2-$) groups. This can likely be explained by the symmetrical addition of an identical polarity group to both ends of the molecular structure, decreasing the polarity of the dinitrile structures. Furthermore, the addition of nonpolar methylene groups between the two nitrile end groups also tends to further decrease the overall polarity of the structure. This relationship is indicative that polarity can be decreased by the utilization of long-chain dinitrile groups. Additionally, changes in the chemical structure have also manifested on other physiochemical properties of the dinitrile solvents, such as viscosity, which increased going from ACN to the dinitrile solvent (ADN) and further increasing with lengthening of the dinitrile chain (SEN).

https://doi.org/10.1021/acs.jpcc.3c00819
J. Phys. Chem. C 2023, 127, 7230−7238

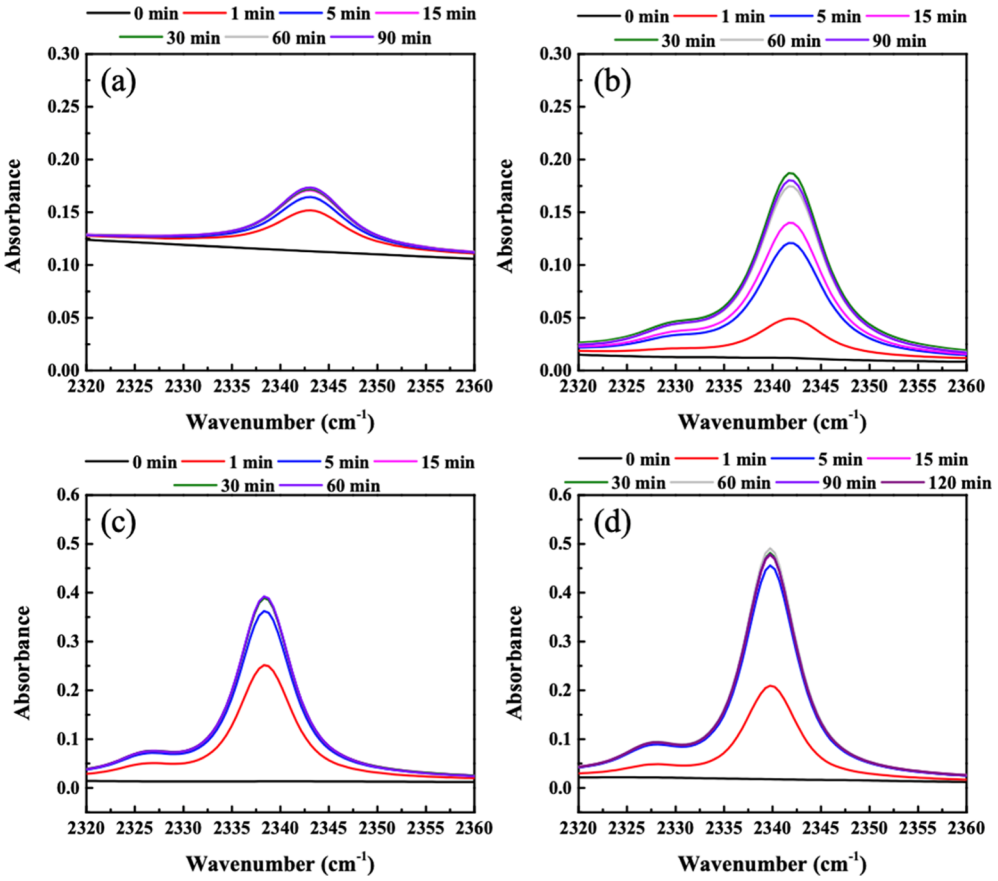

Figure 2. FTIR CO_2 peak spectrum evolution over CO_2 purge times for (a) water, (b) acetonitrile, (c) sebaconitrile, and (d) adiponitrile.

Due to the utilization of the polar salt $TBAPF_6$ for the electrolyte, solubility was expected to decrease along with decreasing solvent polarity. The decreasing solubility trend followed the expected decreasing polarity of the solvents, with salt solubility limit values of >2.5, 1.0, and 0.4 M for ACN, ADN, and SEN, respectively. Conductivity measurements with response to salt concentration were also evaluated, plotted in Figure 1a. The conductivity increased with concentration less than 1 M for all solvents. However, at the 1 M concentration point, the conductivity of ADN plateaued at its solubility limit, while that of ACN reached a maximum and began to decrease afterward. A simple explanation for the exhibited behavior in ACN may be due to increased viscosity of the solution with the addition of the salt past the 1 M point. As more available ions are present with each addition, conductivity naturally increases; however, if the mobility of the ions is hindered, such as with viscosity, a decrease can begin to occur.[9] A more sophisticated explanation is given by Abu-Lebdeh's model of electrolyte solutions which correlates the conductivity of the electrolytes to changes in the structure that can be understood by the solid−liquid, binary (solvent-salt) phase diagram. C_{max} is related to X_{max}, the eutectic composition of molten bulk solvent and solvate or salt in the phase diagram, which has the highest conductivity that decreases due to a diluting effect at both ends of the isotherm.[10−12] However, prior to the 1 M concentration, a decreasing conductivity trend can be seen from ACN > ADN > SEN. As conductivity is related to ionic mobility[6] and the solvents have increasingly hindered mobility of ions from increasing viscosity from ACN < ADN < SEN, the conductivities were expected to decrease in an inversely proportional fashion to the viscosities. Figure 1b displays the conductivity results for the 0.1 M $TBAPF_6$ concentration in all solvents, as well as the corresponding dielectric constant and viscosity values. Notably, a proportional inverse trend between viscosity and conductivity is observed. With the addition of the secondary nitrile group going from ACN to ADN, the viscosity significantly increases by 8.85 cP, while the conductivity decreased by 8.7 mS. A similar trend is seen comparing ADN to SEN, where the viscosity exhibited an increase of 2.64 cP and the conductivity decreased by 0.45 mS.

As viscosity is temperature dependent, conductivity can be improved through increasing temperature. The effect of conductivity with respect to temperature variation between 20 and 80 °C is shown in Figure 1c for ADN solutions for 0.1, 0.4, and 0.7 M $TBAPF_6$ concentrations. ADN was selected for the studies due to its increased CO_2 solubility, as seen in the next section, as well as improved thermal properties, lower cost, and increased availability compared to other solvents. In Figure 1c, evidence of rising conductivity with higher temperatures is observed by the rising slope, as ionic mobility is increased. With increasing concentration, conductivity rose proportionally following the trend observed in Figure 1c. As such, through the combined effect, the slope rose with increasing concentration. However, through estimation with the trendline of 0.1 M $TBAPF_6$ concentration, a temperature of approximately 1933 °C would be required to achieve the 9.43 mS conductivity exhibited by ACN at the same concentration. Similarly, for the concentrations of 0.4 and 0.7 M $TBAPF_6$, the required temperatures would be 1259 and 975 °C, respectively. Therefore, these results indicate that feasible increases in

https://doi.org/10.1021/acs.jpcc.3c00819
J. Phys. Chem. C 2023, 127, 7230−7238

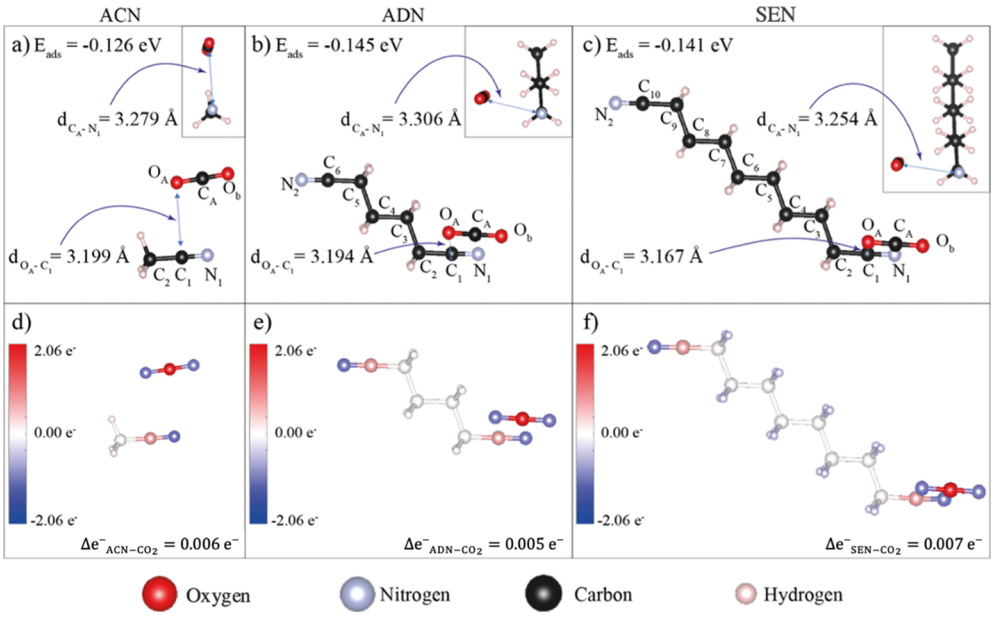

Figure 3. ACN, ADN, and SEN are depicted from left to right columns, where the top file shows the most favorable adsorption case for (a) ACN, (b) ADN and (c) SEN, and the bottom file shows the atomic charge transference for (d) ACN, (e) ADN and (f) SEN. Δe^- is the total charge transferred from the nitrile-based molecules to the CO_2 molecule, indicating that carbon dioxide became slightly more negative.

temperature are not sufficient for the conductivity of ADN to reach that of ACN. Figure 1d shows the data translated into a linearized Arrhenius plot. The derived activation energies and pre-exponential factors were determined from the linearized data. The activation energies were 5.27, 6.55, and 8.93 kJ/mol for the 0.1, 0.4, and 0.7 M concentrations, respectively. This indicates a more hindered transport process due to the increased ion−ion and ion−dipole interactions. This is in contrast with most electrolyte solutions that show a decrease in activation energy below the C_{max}, the concentration with the highest conductivity that is correlated with the eutectic composition in the liquid−solid binary phase diagram according to Abu-Lebdeh's model of electrolyte solutions.[10,11] The determined pre-exponential factors were 5.45, 25.52, and 80.19 mS with 0.1, 0.4, and 0.7 M concentrations, respectively. This is in line with what is observed for aqueous electrolyte solutions.

3.2. CO_2 Solubility in Electrolytic Solvents. The CO_2 solubility in the electrolytic solvents was evaluated through quantified FTIR spectra, shown in Figure 2a−d. The dissolved CO_2 presented a peak at ∼2340−2350 cm^{-1}, which is the same range where no peak was observed previous to the purging of CO_2 into the solvents.

The solubility of CO_2 was expected to increase with decreasing polarity of the electrolyte solvents as CO_2 is a nonpolar molecule. It was observed that water (Figure 2a) indeed displayed the smallest CO_2 peak with an absorbance peak of approximately 0.1, when the background without purging is subtracted. Meanwhile, ACN (Figure 2b) displayed an absorbance peak of ∼0.2 and a visibly broader peak. Then, the dinitriles, SEN and ADN (Figure 2c,d), displayed absorbances of ∼0.38 and ∼0.5, respectively. The result of the normalized integrated areas (Supporting Information, Figures S4 and S5 along with Tables S1−S3) were proportional to the observed absorbance trends with the respective values of 0.002, 0.005, 0.010, and 0.009 for water, ACN, ADN, and SEN. The determined CO_2 solubility concentration values were 40,[5] 270,[5] 582, and 503 mM. This represents an increase by a factor of 14 in solubility going from water to dinitrile and two times increase going from acetonitrile to a dinitrile solvent (ADN). However, even though SEN resulted in an increased CO_2 solubility compared to water and ACN, its solubility is lightly less than that of ADN. This potentially indicates a limit to the effect of hydrophobicity or is attributed to other factors, such as low fluidity of the bulk solvent. Notably, the results for all solvents apart from SEN followed the expected trend with respect to decreasing polarity. As such, the results indicate that the addition of a secondary nitrile group increases the CO_2 solubility. Meanwhile, the increase of the chain length of the dinitrile chains, going from ADN to SEN, slightly hinders the CO_2 solubility. Another potential theory for the decrease could be attributed to intermolecular interactions. Based on the molecules, the number of nitrile groups per 1 mL of solvent were calculated as 1.15×10^{22}, 1.08×10^{22}, and 0.67×10^{22}, respectively, for ACN, ADN, and SEN. As such, based on CO_2 solubility decreasing with smaller number of available nitrile groups, this could be indicative of CO_2 possessing an affinity toward these groups rather than methylene groups, which increased in availability with chain length.

To shed light on these possible scenarios, a preliminary and simplified study of the CO_2 molecule interaction within the nitrile-based molecules was performed at an atomistic level as modeled by density functional theory (DFT). All possible CO_2 adsorption sites and molecule configurations were considered for each ACN, ADN, and SEN molecule (see DFT results in the Supporting Information). Our results showed that the CO_2 adsorption is a thermodynamically favorable process, being the most stable on the site of the nitrile groups (see Table S4 in Supporting Information). Figure 3 shows only the most stable adsorption configuration and its atomic charge distribution for each case. The most significant geometrical difference in between the dinitrile cases is in the $d_{C_A-N_1}$ and $d_{O_A-C_1}$ distances with decreases of about 2.7 and 0.8% from the interaction with ADN to SEN, respectively. This could indicate that increasing

https://doi.org/10.1021/acs.jpcc.3c00819
J. Phys. Chem. C 2023, 127, 7230−7238

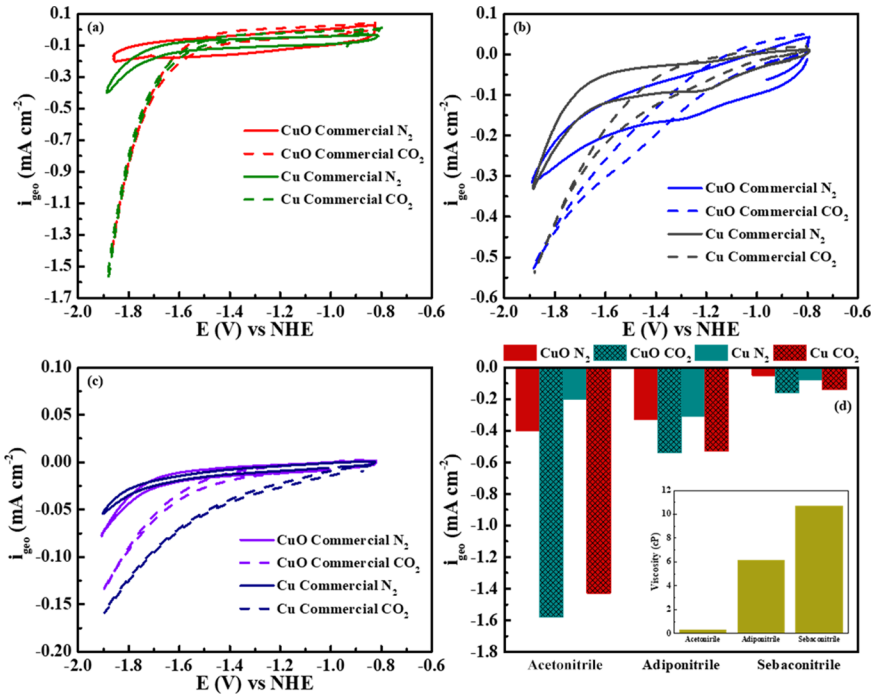

Figure 4. Cyclic voltammograms of CuO and Cu NP catalysts for 0.1 M TBAPF6 in (a) acetonitrile, (b) adiponitrile, and (c) sebaconitrile at 50 mV s^{-1} scan rate (fifth stable cycle). (d) Summary of the maximum current densities of the CVs under a potential of −1.82 V vs NHE with the dynamic viscosity values.

the number of methylene groups decreases the CO_2-nitrile interaction distance. Regarding the CO_2 solubility results, a similar trend was displayed by the adsorption energy (E_{ads}), where the most stable E_{ads} amounts were −0.126, −0.145, and −0.141 eV for ACN, ADN, and SEN cases, respectively (a more negative value indicates more stability). For each ACN, ADN, and SEN case, all E_{ads} results showed that CO_2 preferred to interact with the nitrile groups rather than methylene groups (see Table S4 in Supporting Information). This trend was in line with the idea that the CO_2 solubility results could be, in part, due of the number of nitrile groups per 1 mL of solvent, as aforementioned. It can be seen from charge distribution in Figure 3d−f that ACN is the most polar molecule of the three nitrile molecules. There is no distinguishable difference between the charge distribution of the nitrile groups for the ADN and SEN molecules, which would suggest that there is no appreciable difference in their polarity.

In good agreement with the E_{ads} results, the density of state (DOS) curves for the CO_2 molecule after adsorption showed a shift to lower energies, which is consistent with stabilization of the system. These results reveal that adsorption is a favorable process. Also, a small interaction between the molecules appeared in all cases (green arrows on Figure S6 in Supporting Information). In addition to these results, a negligible amount of charge transfer from the ACN, ADN, and SEN molecules to CO_2 (a lower amount than 0.01 eV in all cases) could be indicative of covalent interaction.

In the case of ADN and SEN, a second CO_2 was adsorbed at the remaining nitrile group (see Figure S7 in Supporting Information), showing an E_{ads} value that is exactly two times of the case with only one CO_2. This result showed that there is no intramolecular CO_2−CO_2 interaction present, which suggests that only the interaction between the molecules of mono- and dinitrile solvents could be responsible for this observed trend and have to be taken into account in future studies. The bond order calculations showed a good correlation with the charge transference, electronic structure, and geometrical considerations. These results are consistent with a physisorption process (Table S5 in Supporting Information).

3.3. Electrochemical Results. Depicted in Figure S10a−d are the activities in relation to the potentials under N_2 purge for CuO commercial (CuO NPs) and Cu commercial (Cu NPs). The detailed information of TEM and XRD characterizations for the catalysts are shown in the Supporting Information, Figures S8 and S9. Under N_2 purge conditions, the measured currents are mainly attributed to the competing HER, as small traces of water at the ppm level have been found to impact the activity by serving as proton donors in the reaction.[13] Although the solvents and salts were dried prior to mixing of the electrolyte solution, traces of water could have remained in the components or could have been introduced from the atmospheric humidity. In Figure S3, the FT-IR peak spectrum of all solvents and water without CO_2 purge are displayed. Notably, ADN displays peaks at 1630 cm^{-1}, as well as between 3500 and 3700 cm^{-1}, which, respectively, align to the OH scissors and the OH stretch in water. This indicates that a small amount of water was present in the ADN solvent after drying, due to the reduced magnitude of the peaks. However, no other organic solvent showed evidence of peaks occurring in that region. The water content in $TBAPF_6$ after drying was not evaluated and thus could have been a potential source of water contamination in the electrolytes due to its hygroscopic nature.

In Figure S10a,b, a comparison between the aqueous and nitrile electrolytes is done. Current densities decrease from −2.8 and −3.5 mA cm^{-2} in aqueous electrolyte using CuO and Cu nanoparticles, respectively, to values at or below −0.4 mA cm^{-2} in organic electrolytes. Notably, a direct quantified comparison cannot be made as the reduction occurs at a greater potential for organic electrolytes due to the lack of

https://doi.org/10.1021/acs.jpcc.3c00819
J. Phys. Chem. C 2023, 127, 7230−7238

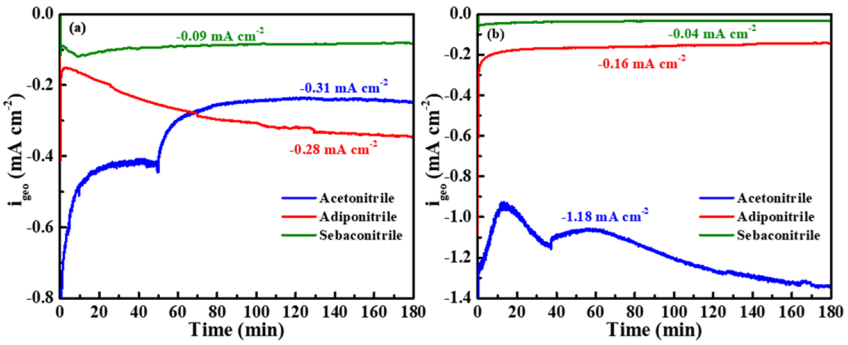

Figure 5. Chronoamperometry plots of (a) CuO commercial nanoparticles and (b) Cu commercial nanoparticles at −1.7 vs NHE potential for 3 h in acetonitrile, adiponitrile, and sebaconitrile electrolytes. The average values of the CA results are displayed in the boxes next to the plots.

availability of H^+.[5,6] However, it can still be observed that suppression of the HER occurs from aqueous to organic solvent electrolytes, indicating a reduction of H^+ ion availability with the use of aprotic organic solvents. In Figure S10c,d, the current density differences under N_2 purge in ACN, ADN, and SEN electrolytes are observed in more detail for both Cu and CuO NPs. The current densities displayed for the CuO catalyst were −0.4, −0.33, and −0.05 mA cm^{-2} for ACN, ADN, and SEN, respectively. For the Cu catalyst, the values were −0.2, −0.31, and −0.08 mA cm^{-2} in the corresponding order of ACN, ADN, and SEN. Comparatively, a significant deviation was not observed in the activities of ADN and SEN between the two catalysts with only a change between 0.02 and 0.03 mA cm^{-2}. Meanwhile, ACN displayed a decrease in the activity of 0.2 mA cm^{-2} going from CuO to Cu catalyst.

Figure 4a−c displays the current densities as a function of potential for the combined effect of both HER and CO_2ER with the introduction of CO_2 purge in ACN, ADN, and SEN for both CuO and Cu commercial nanoparticle catalysts. Additionally, a comparison between the CO_2 purge current densities in the organic solvent electrolytes with the aqueous electrolyte can be observed in Figure S11a,b for both commercial catalysts. It can be observed that a more negative potential is required for the reduction to occur in the organic electrolytes, as it follows the $CO_2^{-\bullet}$ anion pathway due to the lack of H^+ ion availability. Meanwhile, Figure 4d demonstrates a summary of the maximum current densities of all organic solvents. The difference between the N_2 purge and the CO_2 purge current densities provides an estimate of the activity of the CO_2ER. The greatest difference between these was observed in the maximum points of the ACN, for both catalysts. In ACN, the current densities increased from −0.2 to −1.4 mA cm^{-2} and from −0.4 to −1.6 mA cm^{-2} in Cu and CuO, respectively. In ADN, the observed increase was from −0.31 to −0.53 mA cm^{-2} and −0.33 to −0.54 mA cm^{-2} in Cu and CuO, respectively. Finally in SEN, the increases in current densities occurred from −0.05 to −0.16 mA cm^{-2} and −0.08 to −0.14 mA cm^{-2} corresponding to Cu and CuO, respectively. It had been expected that the electrochemical activity trend would proportionally follow the observed trends of CO_2 solubility in the solvents. However, as observed in Figure 4d, a proportional decreasing trend from more to less negative CO_2ER activities can be observed from ACN > ADN > SEN with both catalysts. This trend aligns with the observed behavior in conductivity, which was related to increasing viscosity of the solvents. Therefore, although CO_2 solubility is observed to be increasing from the mononitrile to the dinitrile structures, the ion mobility hindrance overshadows any improvements that were expected from increased CO_2 solubility. A test was conducted to ensure that the purging time of 15 min was sufficient to saturate the cell, where CO_2 purging was extended from 15 min to 3 h (Figure S12). The results demonstrated that minimal activity change was observed and thus lack of dissolved CO_2 was not evident in the electrochemical experiments.

In addition to CV tests, 3 h CAs were also conducted to observe the effect on the catalytic stability. Figure 5a,b displays the current densities over 3 h with a held potential at −1.7 V vs NHE. CVs conducted before and after the CA studies are also shown in (Figure S13). It was found that the average current densities were −0.31, −0.28, and −0.09 mA cm^{-2} for ACN, ADN, and SEN, respectively, utilizing the CuO commercial catalyst. Meanwhile, the values for the Cu commercial catalyst were found to be −1.18, −0.16, and −0.04 mA cm^{-2} for ACN, ADN, and SEN, respectively. Overall, current density value trends in the order of ACN > ADN > SEN were again observed for both catalysts, supporting again the role of the viscosity effects hindering conductivity and thus performance, despite increased CO_2 solubility. Comparing behavior over time, the SEN trends with both catalysts were mostly stable over the 3 h time period, with CuO having a more negative average current density value. Notably a slight increase in activity with CuO catalyst using SEN was observed when comparing the CV results before and post CA measurements (Figure S13e). In ADN, relative stability was seen with the Cu catalyst performance. However, with the use of CuO in ADN, the activity was observed to be trending toward higher negative values over time. The increase occurred from −0.15 to −0.35 mA cm^{-2}, observing an increase in the activity by a factor of 2.3 over the 3 h period with relative stabilization occurring at the end. Finally, in ACN, the initial trend in the first 60 min was unstable for both catalysts. In CuO, relative stability was observed in the first 50 min with a −0.42 mA cm^{-2} current density. However, at the 50 min mark, a decrease in activity was observed to reach another stability point at −0.24 mA cm^{-2}, decreasing by a factor of 0.57. In Cu, an overall better performance was observed with the lowest current density values. The trend was unstable for the first 60 min, after which the current density trend increased, ending with a value of −1.34 mA cm^{-2} at the 3 h mark.

The CA results point toward the CuO catalyst interactions with the dinitrile solvents showing improving performance over time and decreasing with Cu, which is opposite to the catalyst results in ACN. As such, changes in intermediate stabilization seem to be occurring between Cu and CuO going

https://doi.org/10.1021/acs.jpcc.3c00819
J. Phys. Chem. C 2023, 127, 7230−7238

from mononitrile to dinitrile solvents. Further insights into this theory would need to be evaluated using further modeling and characterization of the catalyst surface intermediates and electrolyte interactions. Increases in activity over time may also be attributed to restructuring of the catalyst due to the electrolyte environment, improving interactions on the catalyst surface. However, image characterization techniques to observe the catalytic evolution over time would be required to confirm this in the future. Additionally, product formation may change over time as well; thus, product analysis will also be required in the future to understand in more detail the electrolytic effects on product distribution. As such, future work will entail the development of a small-scale flow cell reactor to allow for in situ analysis, as well as for product measurements, with a greater electrode surface area compared to what is currently being used.

4. CONCLUSIONS

The results of the $TBAPF_6$ polar salt solubility in the solvents follows proportionally the polarity trend from ACN > ADN > SEN, as observed from the dielectric constant values. In line with the observed polarity, the CO_2 solubility results demonstrate an increase in solubility from ACN to ADN. However, a decrease in CO_2 solubility with increasing chain length with the use of SEN is observed. This demonstrates that the addition of a second nitrile end group improved CO_2 solubility through the reduced polarity effect from ACN to ADN. Meanwhile, the increasing chain length effect from ADN to SEN resulting in decreased CO_2 solubility indicates that intermolecular interactions between CO_2 and nitrile groups rather than between CO_2 and methylene groups are likely at play. The preliminary DFT computations, in good agreement with the experimental results, show that CO_2 adsorption is a thermodynamically favorable process, where the preferable interaction occurs at the nitrile groups. Also, the adsorption energies trend is similar to the solubility experimental trend. All these results are consistent with the electronic structure, charge transfer, bond distance, and BO. From the electrochemical results, evidence of HER suppression was observed in the organic electrolytes compared to the aqueous electrolyte. However, contrary to CO_2 solubility results, the CO_2ER activity decreased from ACN to ADN and further with SEN. The trend is also inversely proportional to increasing viscosity from ACN to ADN and to SEN, aligning with the decreasing conductivity trend observed in the order of ACN > ADN > SEN. Chronoamperometry activity results also follow the decreasing trend from ACN > ADN > SEN. Notably, increasing activity was observed with the use of CuO in ADN and SEN over time, with ADN showing more negative current densities compared to ACN.

ASSOCIATED CONTENT

Supporting Information

The Supporting Information is available free of charge at https://pubs.acs.org/doi/10.1021/acs.jpcc.3c00819.

Details on the experimental and computational methods, detailed physiochemical characterization of CuO and Cu nanoparticles, reference electrode calibration, additional FTIR data, and electrochemical measurements (PDF)

AUTHOR INFORMATION

Corresponding Author

Yaser Abu-Lebdeh − *Energy, Mining and Environment Research Centre, National Research Council of Canada, Ottawa, Ontario K1A 0R6, Canada;* orcid.org/0000-0001-8936-4238; Phone: +1 (613)949-4184; Email: Yaser.Abu-Lebdeh@cnrc-nrc.gc.ca; Fax: +1 (613) 991-2384

Authors

Tatiana Morin Caamano − *Department of Chemical and Biological Engineering, Center for Catalysis Research and Innovation (CCRI), University of Ottawa, Ottawa, Ontario K1N 6N5, Canada*

Mohamed S. E. Houache − *Energy, Mining and Environment Research Centre, National Research Council of Canada, Ottawa, Ontario K1A 0R6, Canada;* orcid.org/0000-0002-3944-9660

Mario G. Sandoval − *Department of Mechanical Engineering, Center for Research in Photonics, University of Ottawa, Ottawa, Ontario K1N 6N5, Canada*

Martin Couillard − *Energy, Mining and Environment Research Centre, National Research Council of Canada, Ottawa, Ontario K1A 0R6, Canada*

Arnaud Weck − *Department of Mechanical Engineering, Center for Research in Photonics, University of Ottawa, Ottawa, Ontario K1N 6N5, Canada*

Elena. A. Baranova − *Department of Chemical and Biological Engineering, Center for Catalysis Research and Innovation (CCRI), University of Ottawa, Ottawa, Ontario K1N 6N5, Canada;* orcid.org/0000-0001-5993-2740

Complete contact information is available at: https://pubs.acs.org/10.1021/acs.jpcc.3c00819

Notes

The authors declare no competing financial interest.

ACKNOWLEDGMENTS

This research was enabled in part by support provided by the Natural Resources of Canada (NRC) under the Materials for Clean Fuel program (A1-017184) and the Digital Research Alliance of Canada (alliancecan.ca). We also acknowledge Prof. Paula V. Jasen and Prof. Alfredo Juan for their help with DFT calculation discussion.

REFERENCES

(1) Birhanu, M. K.; Tsai, M.-C.; Kahsay, A. W.; Chen, C.-T.; Zeleke, T. S.; Ibrahim, K. B.; Huang, C.-J.; Su, W.-N.; Hwang, B.-J. Copper and Copper-Based Bimetallic Catalysts for Carbon Dioxide Electroreduction. *Adv. Mater. Interfac.* **2018**, *5*, 1800919.

(2) Vasileff, A.; Xu, C.; Jiao, Y.; Zheng, Y.; Qiao, S. Z. Surface and Interface Engineering in Copper-Based Bimetallic Materials for Selective CO2 Electroreduction. *Chem* **2018**, *4*, 1809−1831.

(3) Pörtner, H.-O.; Roberts, D. C.; Tignor, M. M. B.; Poloczanska, E.; Mintenbeck, K.; Alegría, A.; Craig, M.; Langsdorf, S.; Löschke, S.; Möller, V.; Okem, A.; Rama, B. *Climate Change 2022: Impacts, Adaptation, and Vulnerability. Contribution of Working Group II to the Sixth Assessment Report of the Intergovernmental Panel on Climate Change*; IPCC, 2022.

(4) Nitopi, S.; Bertheussen, E.; Scott, S. B.; Liu, X.; Engstfeld, A. K.; Horch, S.; Seger, B.; Stephens, I. E. L.; Chan, K.; Hahn, C.; Nørskov, J. K.; Jaramillo, T. F.; Chorkendorff, I. Progress and Perspectives of Electrochemical CO2 Reduction on Copper in Aqueous Electrolyte. *Chem. Rev.* **2019**, *119*, 7610−7672.

(5) Moura de Salles Pupo, M.; Kortlever, R. Electrolyte Effects on the Electrochemical Reduction of CO 2. *ChemPhysChem* **2019**, *20*, 2926−2935.
(6) König, M.; Vaes, J.; Klemm, E.; Pant, D. Solvents and Supporting Electrolytes in the Electrocatalytic Reduction of CO2. *iScience* **2019**, *19*, 135−160.
(7) Yu, H.; Obrovac, M. N. Quantitative Determination of Carbon Dioxide Content in Organic Electrolytes by Infrared Spectroscopy. *J. Electrochem. Soc.* **2019**, *166*, A2467−A2470.
(8) Duncan, H.; Salem, N.; Abu-Lebdeh, Y. Electrolyte Formulations Based on Dinitrile Solvents for High Voltage Li-Ion Batteries. *J. Electrochem. Soc.* **2013**, *160*, A838−A848.
(9) Young, H. D.; Freedman, R. A.; Ford, A. L. *Sears and Zemansky's University Physics: With Modern Physics*, 13th ed.; Addison-Wesley, 2012.
(10) Yim, C.-H.; Abu-Lebdeh, Y. A. Connection between Phase Diagram, Structure and Ion Transport in Liquid, Aqueous Electrolyte Solutions of Lithium Chloride. *J. Electrochem. Soc.* **2018**, *165*, A547−A556.
(11) Yim, C.-H.; Tam, J.; Soboleski, H.; Abu-Lebdeh, Y. On the Correlation between Free Volume, Phase Diagram and Ionic Conductivity of Aqueous and Non-Aqueous Lithium Battery Electrolyte Solutions over a Wide Concentration Range. *J. Electrochem. Soc.* **2017**, *164*, A1002−A1011.
(12) Franko, C. J.; Yim, C.-H.; Årén, F.; Åvall, G.; Whitfield, P. S.; Johansson, P.; Abu-Lebdeh, Y. A.; Goward, G. R. Concentration Dependent Solution Structure and Transport Mechanism in High Voltage LiTFSI-Adiponitrile Electrolytes. *J. Electrochem. Soc.* **2020**, *167*, 160532.
(13) Figueiredo, M. C.; Ledezma-Yanez, I.; Koper, M. T. M. In Situ Spectroscopic Study of CO2 Electroreduction at Copper Electrodes in Acetonitrile. *ACS Catal.* **2016**, *6*, 2382−2392.

https://doi.org/10.1021/acs.jpcc.3c00819
J. Phys. Chem. C 2023, 127, 7230−7238